Structural, electronic, and magnetic properties of math xmlns="http://www.w3.org/1998/Math/MathML">msub>mi >CrTe/mi>mn>2/mn>/msub>/math>

Yuhang Liu, Sohee Kwon, George J. de Coster, Roger K. Lake, and Mahesh R. Neupane

Phys. Rev. Materials **6**, 084004 — Published 19 August 2022

DOI: 10.1103/PhysRevMaterials.6.084004

Structural, electronic, and magnetic properties of $CrTe_2$

Yuhang Liu,[1,*] Sohee Kwon,[1] George J. de Coster,[2] Roger K. Lake,[1,†] and Mahesh R. Neupane[1,2,‡]

[1] *Laboratory for Terahertz & Terascale Electronics (LATTE), Department of Electrical and Computer Engineering, University of California-Riverside, Riverside, CA, 92521, USA*

[2] *DEVCOM Army Research Laboratory, 2800 Powder Mill Rd, Adelphi, MD, 20783, USA*

Two dimensional chromium ditelluride ($CrTe_2$) is a promising ferromagnetic layered material that exhibits long-range ferromagnetic ordering in the monolayer limit. The formation energies of the different possible structural phases (1T, 1H, 2H) calculated from density functional theory (DFT) show that the 1T phase is the ground state, and the energetic transition barriers between the phases, calculated by the nudged elastic band method, are large, on the order of 0.5 eV. The self-consistent Hubbard U correction parameters are calculated for all the phases of $CrTe_2$. The calculated magnetic moment of 1T-$CrTe_2$ with ≥ 2 layers lies in the plane, whereas the magnetic moment of a monolayer is out-of-plane. Band filling and tensile bi-axial strain cause the magnetic moment of a monolayer to switch from out-of-plane to in-plane, and compressive bi-axial strain in a bilayer causes the magnetic moment to switch from in-plane to out-of-plane. The magnetic anisotropy is shown to originate from the large spin orbit coupling (SOC) of the Te atoms and the anisotropy of the exchange coupling constants J_{xy} and J_z in an XXZ type Hamiltonian. Renormalized spin wave theory using experimental values for the magnetic anisotropy energy and Curie temperatures provides a range of values for the nearest neighbor exchange coupling.

I. INTRODUCTION

The recent discovery of monolayer two-dimensional (2D) ferromagnetic (FM) material [1, 2], the compatibility of 2D FM materials with other 2D materials, and their susceptibility to external control of their magnetic properties have made 2D FM materials a topic of high current interest. For example, the magnetic anisotropy can be controlled by applying an external electric field [3], strain [4], and band filling [5]. The ground state magnetic ordering can be switched among ferromagnetic (FM), anti-ferromagnetic (AFM), collinear, and noncollinear by stacking pattern [6], strain [7], and electric field [8, 9]. Moreover, the formation of heterostructures with other 2D materials, breaks time reversal symmetry, which can be exploited for valleytronics [10] or the creation of a Chern insulator [11].

A relatively new class of layered magnetic materials such as $CrTe_2$, CrI_2 and $CrGeTe_3$ have extended the applicability of the layered materials in the field of spintronics [12]. One material of particular interest is $CrTe_2$ in which Cr hexagonal planes are sandwiched by Te layers. Several studies [13, 14] suggested the non-magnetic 2H phase was the ground state, whereas recent studies all find the 1T phase to be the ground state [15–20]. 1T-$CrTe_2$ has one of the highest Curie temperatures among the 2D magnetic materials. The discovery that bulk 1T-$CrTe_2$ is a layered metallic ferromagnet with a Curie temperature of ~ 310 K [15], led to a number of further studies. Mechanical exfoliation of 1T-$CrTe_2$ with either h-BN or Pt encapsulation in a glove box produced samples in which easy-plane ferromagnetism was maintained in thin-films down to ~ 8 nm while maintaining a Curie temperature above 300K [16]. This study also showed that $CrTe_2$ rapidly oxidizes in ambient conditions and that the pristine Raman peaks at 100 cm^{-1} and 134 cm^{-1} shift to 125 cm^{-1} and 145 cm^{-1} after a few hours in air [16]. A number of studies of epitaxial grown material quickly followed. Thin film 1T-$CrTe_2$ was grown by molecular beam epitaxy (MBE) on bilayer graphene (BLG)/SiC and capped with a 5 nm Te layer to prevent oxidation [17]. Ultrathin films (≤ 7 monolayers (ML)) posessed perpendicular magnetic anisotropy (PMA) with T_c dropping from 300 K for thicker films down to 200 K for a monolayer. A large PMA constant of $K_u = 5.63 \times 10^6$ erg/cm^3 was measured for a 7 ML film. In a separate work, this value of K_u was also found for 80 nm thick films of $Cr_{1.3}Te_2$ [21]. In thin films of 1T-$CrTe_2$ grown by chemical vapor deposition (CVD) on SiO_2, the magnetic easy axis changed from in-plane to perpendicular as the thickness was reduced below approximately 10 nm (≈ 17 MLs) [18]. Reflectance magneto circular dichroism measurements showed that T_c increased from approximately 165 K to 212 K as the film thickness decreased from 48 nm to 7.5 nm. This last trend of *increasing* T_c with *decreasing* film thickness is unique to these samples and experiments. The majority of the data in this study was taken from oxidized samples based on the Raman peaks at 123 cm^{-1} and 143 cm^{-1}, however a comparison was made between samples with and without h-BN encapsulation; the values for T_c remained essentially the same, and both sets of films exhibited strong PMA [18]. The authors theoretically found that the sign of the magnetic anisotropy energy (MAE) in ML 1T-$CrTe_2$ switches from in-plane to out-of-plane with increasing magnitude of the on-site Coulomb potential (U), with switching occurring at $U \sim 3.2$ eV; and they discuss the possibility

* yliu446@ucr.edu
† rlake@ece.ucr.edu
‡ mahesh.r.neupane.civ@army.mil

that thinner samples provide less screening, larger electrostatic interaction with the substrate, larger values of U, and thus PMA [18]. MBE grown 1T-$CrTe_2$ on (111) GaAs exhibited a Curie temperature that dropped from $T_c = 205$ K for a 35 ML film to 191 K for a 4 ML film, and, unique to these samples, all thicknesses exhibited PMA [19]. No information on a capping layer or other protection from oxidation was provided [19]. A most recent study of MBE grown 1T-$CrTe_2$ on BLG/SiC found that ML 1T-$CrTe_2$ had a zigzag AFM (z-AFM) ground state accompanied by a 2×1 reconstruction of the lattice resulting from relatively large substrate induced strain (-5% along a_1 and +3% along a_2) [22].

The intense interest in 1T-$CrTe_2$ also motivated many theoretical investigations based on density functional theory calculations. Calculations using the Perdew-Burke-Emzerhof (PBE) functional [23] without a Hubbard U correction or spin orbit coupling found that 1% compressive strain caused ML 1T-$CrTe_2$ to transition from an FM to an AFM ground state [24]. Simulations of ML 1T-$CrTe_2$ with the all electron code WIEN2k [25] using the PBE functional found imaginary modes in the phonon spectrum which were removed in a $\sqrt{3}\times\sqrt{3}$ charge density wave (CDW) state [26]. In both the normal and CDW phase, tensile strain was required to obtain PMA, and the magnetic anisotropy swtitched from in-plane to out-of-plane for a lattice constant of $\gtrsim 3.8$ Å in the CDW phase and $\gtrsim 3.86$ Å in the normal phase [26]. PBE+U calculations, with $U = 2$ eV, found a stable phonon spectrum for ML 1T-$CrTe_2$ and in-plane FM magnetization [27]. The finding of in-plane magnetization results from the use of the value $U = 2$ eV [18]. PBE level calculations without a Hubbard U correction found an AFM ground state for ML 1T-$CrTe_2$, and a reduction of the lattice constant from 3.79 Å in the bulk to 3.68 Å in ML [28]. The ML AFM ground state was attributed to the reduction of the lattice constant. The thickness dependence of the magnetization of 1T-$CrTe_2$ was investigated [29] using the opt-B86b-vdW functional [30] implemented in VASP [31, 32]. The ML ground state was found to be z-AFM with a corresponding reduction of the in-plane lattice constant from ~ 3.8 Å for bulk to ~ 3.57 Å for ML [29]. The FM ML CDW ground state [26] was found to be higher in energy than the z-AFM state. The results are qualitatively similar to those of Ref. [28]. AFM interlayer coupling was found in 2 through 4 MLs, and FM interlayer coupling for 5 MLs or more [29]. PBE-D3+($U = 2$ eV) calculations of bilayer 1T-$CrTe_2$ found a g-type AFM ground state with both intra-layer and inter-layer AFM coupling [33]. Compressive strain greater than 4% caused the interlayer coupling to become FM while the intra-layer coupling remained AFM.

CrI_3 is another 2D magnetic material with many similarities to $CrTe_2$. The Cr ion is in octahedral coordination with the I anions resulting in the same e_g, t_{2g} crystal field splitting and superexchange coupling through the Cr-I-Cr bonds at near 90° bond angles. The origin of the large out-of-plane magnetic anisotropy in CrI_3 has been investigated in detail [34, 35]. It was found that the MAE is primarily from the SOC on the I atoms, and, therefore, anisotropic superexchange is the source of the magnetic anisotropy [34]. Further investigation found that the MAE was very sensitive to the deviation of the dihedral angle θ_D between the plane formed by the Cr-I-Cr bonds and a vertical plane through the Cr-Cr pair [35], which is a measure of the trigonal distortion of the edge-sharing $CrTe_6$ octahedra. In the undistorted octahedron, the dihedral angle $\theta_{O_h} \approx 35.3°$, and the deviation is defined as $\delta\theta \equiv \theta_{O_h} - \theta_D$. In CrI_3, positive values for $\delta\theta_D$ resulted in out-of-plane magnetic anisotropy and negative values resulted in in-plane magnetic anisotropy.

The variety of different and contradicting experimental data for 1T-$CrTe_2$ originating from different growth conditions and substrates indicates a sensitivity of the thin layer material to external perturbations such as strain, band filling and screening. The variety of different and contradictory theoretical predictions resulting from different models and, particularly, from the use of different values of U possibly indicate a sensitivity to screening, which is affected by different environments as discussed in [18]. In few monolayer films, both the interlayer magnetic coupling and the sign of the magnetic anisotropy are affected in incompatible ways by the value of U. For few layer films, small U values give, what appears to be at this time, the experimentally correct sign of the interlayer magnetic coupling coupling (i.e. FM), but the incorrect sign for the magnetic anisotropy (i.e. prediction of easy-plane magnetic anisotropy). Conversely, larger values of U predict the correct magnetic anisotropy (PMA), but the incorrect interlayer magnetic coupling (i.e. AFM). Thus, to address the question of the magnetic anisotropy in a monolayer, a value for U must be chosen that reproduces the observed magnetic anisotropy, which, experimentally, is found to be out-of-plane.

In this work, we first quantify the energy differences and energy barriers separating the different crystallographic phases: 1T, 1H, and 2H. We then focus on the magnetic anisotropy of bilayer and monolayer 1T-$CrTe_2$ and understand how it is affected by strain and band filling. We investigate the source of the magnetic anisotropy originating from the large SOC of the Te atoms. Based on the insights gained from prior work on CrI_3 [34, 35], we analyze the SOC matrix elements and distortion of dihedral angle, and their relationships to the sign of the MAE. Finite temperature long range magnetic order in 2D monolayer 1T-$CrTe_2$ is subject to the Mermin-Wagner theorem [36]. As such, an energy gap is required in the magnon excitation spectrum to prevent the magnetic order from being destroyed by thermal fluctuations. This energy gap results from the magnetic anisotropy. The interdependence of the MAE, exchange coupling, and Curie temperature in ML 1T-$CrTe_2$, is analyzed using renormalized spin wave theory (RSWT) [37]. RSWT provides a mean field self-consistent calculation of the magnon mode occupation and the average magnetic mo-

ment as a function of temperature. Examples of RSWT applied to other 2D magnetic materials can be found in Refs[2, 34, 38]. Finally, an inverse calculation is performed in which the experimentally measured value for T_c is used to determine all pairs of values for the MAE and exchange coupling constants that result in T_c.

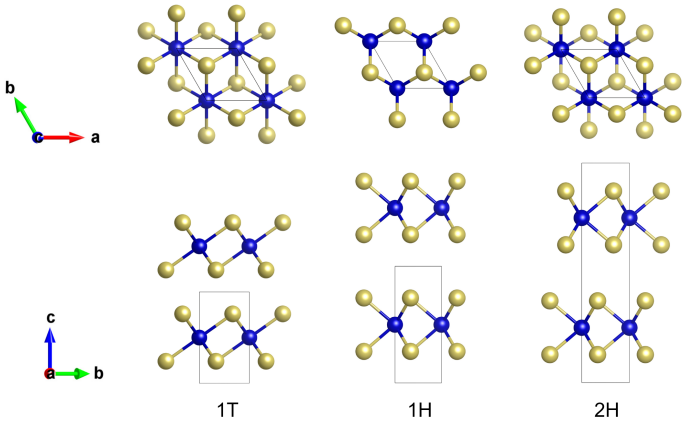

FIG. 1. Top and lateral views of 1T, 1H, and 2H phases of $CrTe_2$. The unit cells are shown by the thin lines. Blue and golden balls represent Cr and Te atoms, respectively. The 1T phase contains one formula unit (f.u.) per unit cell in a hexagonal lattice belonging to the $P\bar{3}m1$ space group with each Cr atom surrounded by Te atoms in octahedral coordination. The 1H and 2H phases are hexagonal, trigonal prismatic, and the difference between the two phases is in their interlayer stacking. In the 1H structure, layers are stacked directly on top of each other so that the 1H structure contains 1 f.u. / unit cell and belongs to the $P\bar{6}m2$ space group. The 2H structure contains 2 f.u. / unit cell and belongs to the $P6_3/mmc$ space group.

II. METHOD

The first-principle calculations use spin-polarized density functional theory (DFT) with the projector augmented wave (PAW) [39, 40] method and a plane-wave basis, as implemented in the Vienna ab initio simulation package (VASP) [31, 32]. The Perdew-Burke-Enzerhof's (PBE) [23] version of the generalized gradient approximation (GGA) is used for the exchange-correlation density functional. The vdW corrections are included with the PBE+D3 model [41]. All structural relaxation calculations use the PBE+D3 level of theory. The lattice is fully relaxed until the force on each atom is smaller than 0.001 eV/Å. For finite thickness slabs, 15 Å vacuum layers are added. Energy barriers between the ground state and the metastable states of $CrTe_2$ are determined using the nudged elastic band (NEB) method [42, 43].

For calculation of the electronic and magnetic properties, the Hubbard U correction (PBE+U) [44]. and spin orbit coupling (SOC) are included. The values of the U parameter for the different phases of $CrTe_2$ are calculated using the linear response method [45], and the values are given in Table I. The details of U parameter calculation are provided in the Supplemental Material (SM) [46]. For all calculations of the magnetic properties of 1T-$CrTe_2$, the value of $U = 5.8$ eV is used. With $U = 5.8$ eV, the magnegetic moment per formula unit of 1T-$CrTe_2$ is 3.05 μ_B for monolayer and 3.08 μ_B for bulk. A table of calculated magnetic moments as a function of U is provided in the Supplemental Material (SM) [46]. This method has been used for other 2D Cr based materials such as CrX_3(X = Cl, Br, I) monolayers [47]. 12 valence electrons are included for Cr ($3p^6 3d^5 4s^1$), and 6 valence electrons for Te ($4s^2 sp^4$). The cutoff energy is 500 eV. A 24×24×12 Monkhorst-Pack k-grid mesh [48] for bulk structures and a 28×28×1 mesh for layered structures are used to ensure that the magnetic anisotropy energies are well converged. The Gaussian smearing method is employed with a width of 0.05 eV for the structure, magnetic, and energy barrier calculations for insulating systems. For metallic systems, the Methfessel-Paxton smearing method is employed with a width of 0.05 eV.

TABLE I. U parameters of the Cr atom in $CrTe_2$ calculated from linear response method.

Phases	1T bulk	1H bulk	2H bulk	1T 1L	1H 1L	2H 2L
U (eV)	5.80	5.59	5.85	5.92	5.91	5.59

III. RESULTS AND DISCUSSION

A. Ground state and energy barrier in phase transition

$CrTe_2$ can potentially crystalize into various layered phases such as 1T, $1T_d$, 1H, and 2H phases [49, 50], as illustrated in Fig. 1. The geometry-optimized in-plane lattice constant a and the interlayer distance d for each phase is shown in Table II. Among all of the possible phases, the $1T_d$ phase of $CrTe_2$ in both the bulk and monolayer forms is unstable during the structure optimization step, and hence is excluded from this study. Experimental values are only known for the 1T bulk phase, and our calculated values match well with the experimental ones of $a = 3.7887$ Å and $c = 6.0955$ Å [15].

To determine the energetic stability of each phase, the formation energy E_{form} is calculated from the energy difference between the material and isolated atoms per chemical formula, which is defined as

$$E_{form} = E_{total} - \sum_{i}^{n} E_i \quad (1)$$

where E_{total} is the total energy of the material, E_i is the energy of a single constituent atom, and n is the total number of atoms in the unit cell of the material. A more

negative E_{form} corresponds to a more stable system. As shown in the Table. II, the 1T phase is the ground state for both the bulk and the monolayer forms. Quantitatively, the formation energy of the 1T bulk phase is lower than those of the 2H and 1H phases by 0.30 and 0.40 eV, respectively.

TABLE II. Formation Energies E_{form} (eV) and relaxed lattice constants for different phases of $CrTe_2$ in bulk, monolayer (1L) and bilayer (2L) geometries. For the bilayer structure, c corresponds to the interlayer Cr-Cr distance.

Phases	E_{form}	a	c
1T bulk	-10.44	3.787	5.967
1T 2L	-10.18	3.759	-
1T 1L	-10.09	3.692	-
1H bulk	-10.04	3.491	7.493
1H 1L	-9.75	3.646	-
2H bulk	-10.14	3.498	6.951
2H 2L	-9.98	3.493	7.001

The energetic barriers separating the ground state from the metastable states, calculated from the NEB method, are shown in Fig. 2 for (a) bulk and (b) monolayer. The energies of the 1T bulk and monolayer serve as the reference energies and ere set to be 0 eV. The energetic barriers for the bulk phase transitions from 1T to 2H and 1H are 0.99 eV and 0.95 eV, respectively. The energetic barrier for the monolayer transition from 1T to 1H is 0.78 eV. The large magnitudes of energy barriers separating the 1T phase from the other metastable phases combined with the large energy differences of the ground states, indicate that the 1T phase, in both bulk and monolayer forms, should be very stable, and transitions to other phases difficult to achieve.

To verify the stability of 1T phase monolayer, the phonon spectrum is calculated using different U parameters as shown in the Supplemental Material (SM) [46]. As found previously [27], the imaginary modes vanish with the inclusion of a non-zero Hubbard U parameter.

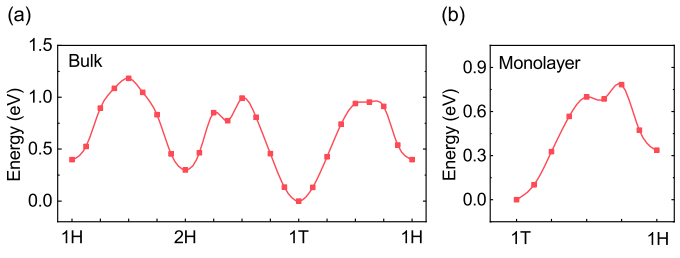

FIG. 2. (a)The energy barrier between 1H, 2H, and 1T phases of bulk $CrTe_2$. (b)The energy barrier between 1T and 1H phases of monolayer $CrTe_2$.

B. The magnetic anisotropy of layered and bulk 1T-$CrTe_2$

The magnetic anisotropy energy plays a crucial role in the stability of the magnetic ordering in low dimensional materials, and there is great interest in controlling it with externally applied fields and strain. We therefore investigate the sensitivity of the MAE to strain and band filling in both few-layer and bulk 1T-$CrTe_2$. Since, the energy differences and energy barriers between the 1T phase and the other phases are large, we only consider the magnetic properties of the 1T phase.

The MAE ($\Delta_{\rm MA}$) is defined as the energy difference between the total energies $E_{\rm total}$ when the magnetization $\mathbf{m}$ lies along the x axis or the z axis, i.e.

$$\Delta_{\rm MA} = E_{\rm total}(\mathbf{m}\|\hat{x}) - E_{\rm total}(\mathbf{m}\|\hat{z}). \quad (2)$$

As shown in the Table III, in the FM ground state, the magnetization easy axis of monolayer 1T-$CrTe_2$ is out-of-plane while the multilayer and bulk 1T-$CrTe_2$ have in-plane magnetic easy axes.

TABLE III. Magnetic anisotropy energies of 1T-$CrTe_2$ in layered and bulk forms.

Structure	MAE per f.u. (meV)	Easy axis
1L	5.56	out-of-plane
2L	-4.15	in-plane
3L	-3.61	in-plane
4L	-2.88	in-plane
5L	-3.37	in-plane
6L	-3.29	in-plane
Bulk	-3.22	in-plane

Device applications require external control of the MAE, so we therefore consider the effects of strain and band filling in monolayer, bilayer, and bulk 1T-$CrTe_2$. Bi-axial strain is simultaneously stretching or compressing the in-plane x-axis and y-axis of the crystal. As shown in the Fig. 3(a) the MAE of a monolayer is sensitive to tensile bi-axial strain, and the MAE of a bilayer is sensitive to compressive bi-axial strain. The easy axis of monolayer 1T-$CrTe_2$ switches from out-of-plane (z-axis) to in-plane (x-axis) at 2.3% bi-axial tensile strain. The easy axis of bilayer 1T-$CrTe_2$ switches from in-plane (x-axis) to out-of-plane (z-axis) at 3% bi-axial compressive strain. The MAE of the bulk structure is relatively insensitive to the applied uni-axial or bi-axial strain. As shown in Fig. 3(b), band filling also switches the magnetic moment of monolayer of 1T-$CrTe_2$ from out-of-plane (z-axis) to in-plane (x-axis). The sign of the MAE switches at a filling of 0.22 electrons per unit cell, corresponding to a sheet carrier concentration of $n_s = 1.9 \times 10^{14}$ cm^{-2}.

To obtain insight into the source of the magnetic anisotropy in 1T-$CrTe_2$, we consider the SOC matrix el-

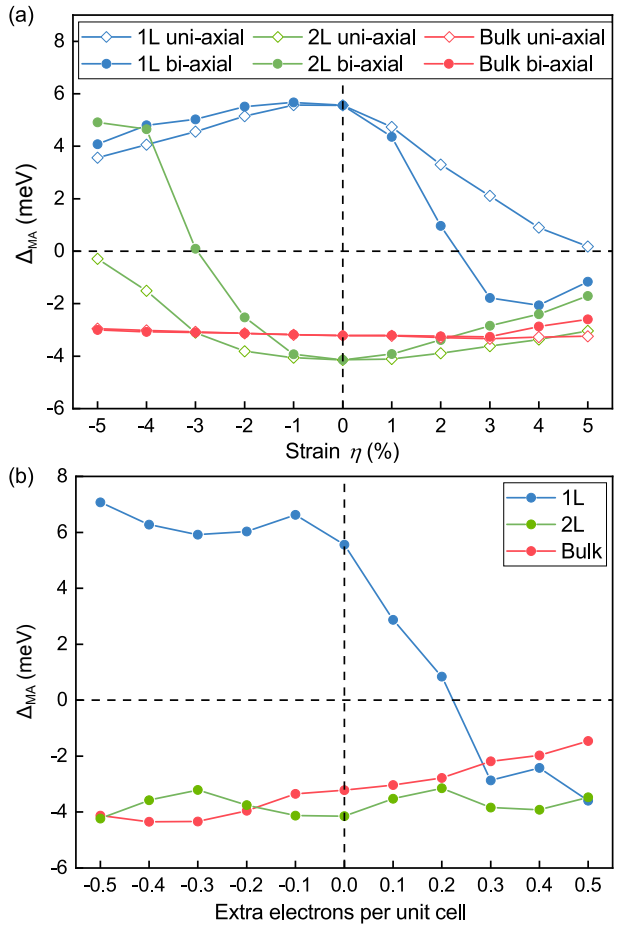

FIG. 3. The MAE as a function of (a) strain and (b) band filling of 1L, 2L, and bulk 1T-$CrTe_2$

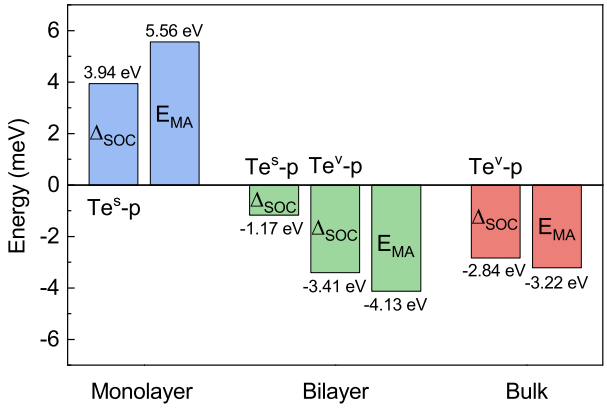

FIG. 4. Magnetic anisotropy energy Δ_{MA} (per f.u.) and difference in SOC energies Δ_{SOC} (per f.u.) of Te-5p orbitals between the x (in-plane) and z (out-of-plane) magnetization orientations. Te^s and Te^v denote the Te atoms on the surface and at the vdW gap of the bilayer, respectively.

ements of Cr-3d and Te-5p orbitals. The Cr d-orbitals' contributions to SOC matrix elements are negligible in comparison with those of the Te p-orbitals, so they will be ignored. We abbreviate the p-orbital matrix elements of the SOC term in the Hamiltonian as $\langle p_i|p_j\rangle$. Similar to the definition of the MAE in Eq. (2), we define

$$\Delta_{\mathrm{SOC}} = E_{\mathrm{SOC}}(\mathbf{m}\|\hat{x}) - E_{\mathrm{SOC}}(\mathbf{m}\|\hat{z}) \tag{3}$$

where E_{SOC} is the energy associated with the SOC matrix elements. In Fig. 4, $E_{\mathrm{SOC}}(\mathbf{m}\|\hat{x},\hat{z})$ is calculated from the sum of the SOC matrix elements, i.e. $E_{\mathrm{SOC}}(\mathbf{m}\|\hat{x},\hat{z}) = (\langle p_y|p_x\rangle + \langle p_y|p_z\rangle + \langle p_x|p_z\rangle)|_{\mathbf{m}\|\hat{x},\hat{z}}$, and the difference Δ_{SOC} is plotted. Fig. 4 shows Δ_{MA} and Δ_{SOC} for monolayer, bilayer and bulk 1T-$CrTe_2$. It is clear that the difference in the SOC energy Δ_{SOC} tracks both the magnitude and sign of the MAE, Δ_{MA}. In the bilayer structure, the Te atoms on the outer surfaces (Te^s) and the ones adjacent to the vdW gap (Te^v) are in different chemical environments, and thus they contribute different amounts to the total MAE.

The changes in individual SOC matrix elements with different magnetization directions are shown in Fig. 5. Here, $\Delta_{\langle p_i|p_j\rangle} = \langle p_i|p_j\rangle|_{\mathbf{m}\|\hat{x}} - \langle p_i|p_j\rangle|_{\mathbf{m}\|\hat{z}}$. In the FM ground state (zero strain) of monolayer 1T-$CrTe_2$, $\langle p_y|p_z\rangle$ contributes the most to Δ_{SOC}, while in the FM ground states of bilayer and bulk, the dominant matrix element is $\langle p_y|p_x\rangle$. A dominant $\Delta_{\langle p_y|p_z\rangle}$ matrix element anisotropy coincides with an out-of-plane easy axis, and a dominant $\Delta_{\langle p_y|p_x\rangle}$ matrix element anisotropy coincides with an in-plane magnetic easy axis.

Fig. 5(a) also shows the effect of strain on the dihedral angle θ_D between the Cr-Te-Cr plane and a vertical plane through the Cr-Cr pair illustrated in Fig. 6. Positive values of $\delta\theta_D = \theta_{O_h} - \theta_D$ correspond to the Cr-Te-Cr plane becoming more vertical. For the monolayer and bilayer, an out-of-plane easy axis occurs at more positive values of $\delta\theta_D$, which is qualitatively consistent with the results for CrI_3 described in Ref. [35], although the dependence is far from linear. For the monolayer In equilibrium, $\delta\theta_D = 2.6°$ is relatively large and positive, the $\Delta_{\langle p_y|p_z\rangle}$ matrix element anisotropy is dominant, and the easy axis is out of plane. For the bilayer in equilibrium, two values of $\delta\theta_D$ are given, one for the Te atom at the surface (1.0°) and one for the Te atom at the van der Waals gap (0.8°). The angles are similar, $\delta\theta_D \sim 1°$, the matrix element anisotropy is dominated by $\Delta_{\langle p_y|p_x\rangle}$, and the easy axis is in plane. As compressive bi-axial strain is applied to the bilayer, $\delta\theta_D$ becomes more positive, the SOC matrix element anisotropy $\Delta_{\langle p_y|p_z\rangle}$ becomes dominant, and the easy plane rotates from in-plane to out-of-plane. For the bulk, compressive strain increases $\delta\theta_D$ to 3.3°, however in the bulk, the anisotropy of the SOC matrix elements and the magnetic anisotropy are insensitive to strain and the dihedral angle.

In terms of percent change, strain has the largest effect on the dihedral angle θ_D, the second largest effect on the Cr-Te-Cr bond angles, and minimal effect on the bond lengths. The distortion produced by in-plane strain or a reduction of the equilibrium in-plane lattice constant is primarily absorbed by the dihedral angles and bond

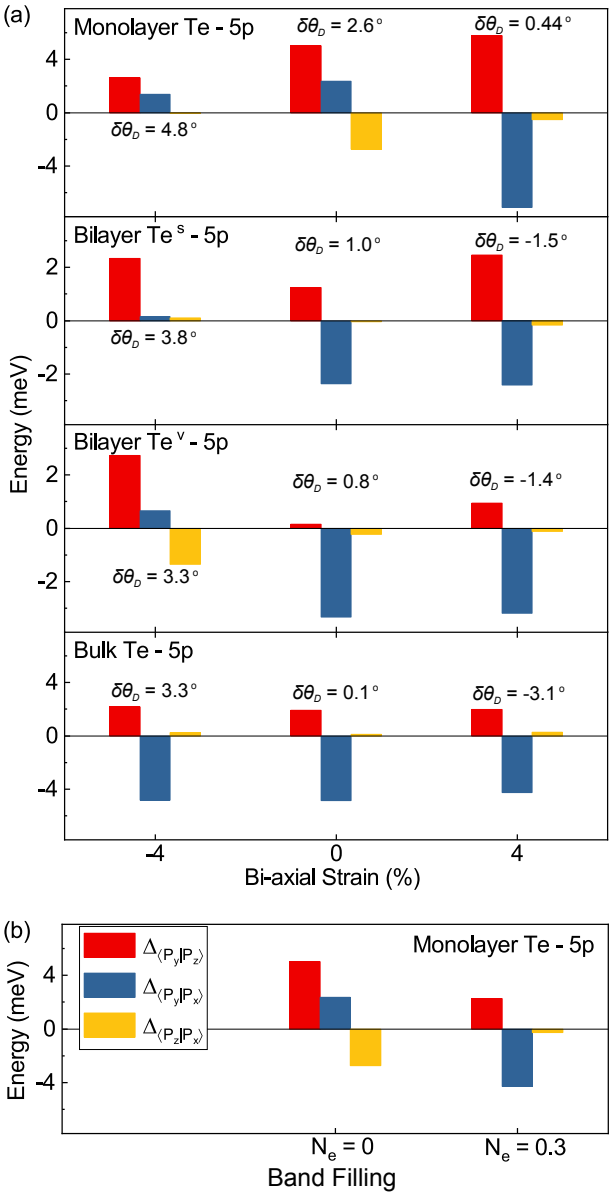

FIG. 5. Difference in SOC matrix elements $\Delta_{\langle p_i|p_j\rangle}$ (per atom) of the Te-5p orbitals. (a) $\Delta_{\langle p_i|p_j\rangle}$ of 1L, 2L, and bulk 1T-$CrTe_2$ versus strain. At each strain, the values for $\delta\theta_D$ are also shown. Positive and negative values of strain correspond to tensile and compressive strain, respectively. For the bilayer, values for Te atoms at the van der Waals gap (Te^v) and Te atoms at the free surface Te^s are shown. (b) $\Delta_{\langle p_i|p_j\rangle}$ of 1L 1T-$CrTe_2$ versus filling. The legend is shown at left.

angles. The decrease in the dihedral angle θ_D is accompanied by a reduction of the Cr-Te-Cr bond angle. For example, the equilibrium in-plane lattice constant of a monolayer (3.692 Å) is 2.5% smaller than that of the bulk (3.787 Å), the Cr-Te-Cr bond angle of the ML (86.3°) is 4% smaller than that of the bulk (89.9°), and the dihedral angle (32.7°) is 7% smaller than that of the bulk (35.2°). Even though the lattice constants of the ML are 2.5% smaller than those of the bulk, the Cr-Te

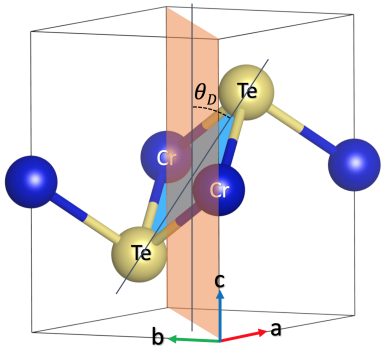

FIG. 6. Illustration of the dihedral angle θ_D between the plane (blue) formed by a Cr-Te-Cr bonds and the perpendicular plane through the Cr-Cr pair (orange).

bond lengths of the ML (2.70 Å) are 0.7% longer than those of the bulk (2.68 Å), since the Te atoms in the ML are free to move into the vacuum. The bond angles and bond lengths of the equilibrium bilayer lie in between those of the monolayer and bulk. The bilayer Cr-$Te^{v(s)}$ bond lengths are 2.68(2.69) Å, the Cr-$Te^{v(s)}$-Cr bond angles are 88.9°(88.5°), and the Cr-$Te^{v(s)}$-Cr dihedral angles are 34.5°(34.3°). When the bilayer is compressed 4% in-plane, the Cr-$Te^{v(s)}$ bond lengths are reduced by 0.6%(0.09%), the Cr-$Te^{v(s)}$-Cr bond angles are reduced by 4.3%(4.8%), and the Cr-$Te^{v(s)}$-Cr dihedral angles are reduced by 9%(10%).

As shown in Fig. 5(b), band filling in the monolayer switches the $\langle p_y|p_x\rangle$ anisotropy from positive to negative, and it decreases the magnitudes of the other two terms. The net result is that the MAE becomes dominated by the $\Delta_{\langle p_y|p_x\rangle}$ term, and the easy axis switches from out-of-plane to in-plane. In the band-filling calculation, the structure is not relaxed after charging, so all of the dihedral angles and bond angles remain the same as in the charge neutral state. Thus, this switching is a purely electronic effect.

C. XXZ Spin Hamiltonian

Magnetic anisotropy originating from the nonmagnetic ligand p electrons is induced by the superexchange mechanism [34, 35, 51] through the Cr-Te-Cr channel. Magnetic anisotropy of this kind is exchange anisotropy, in which the exchange coupling constants of the Heisenberg Hamiltonian depend on the directions of the magnetic moments. A suitable model is the XXZ Hamiltonian in which the the exchange coupling constant for the in-plane component of the spins J_{xy} differs from the out-of-plane component J_z [52]. This model has been shown to apply to CrI_3 [34]. Other sources of anisotropy include single ion anisotropy and dipolar coupling. The effect of dipolar coupling is known to be small, so below, we consider a XXZ type Hamiltonian for the energy per unit cell of monolayer 1T-$CrTe_2$ and also include a single-ion

anisotropy term and an external magnetic field directed in the $\pm z$ direction (along the c axis),

$$H = -J_{xy}\tfrac{1}{N}\sum_{i\neq j}(S_i^x S_j^x + S_i^y S_j^y) - J_z\tfrac{1}{N}\sum_{i\neq j}(S_i^z S_j^z) - K_u\tfrac{1}{N}\sum_j (S_j^z)^2 + g\mu_B B_z \tfrac{1}{N}\sum_j S_j^z. \quad (4)$$

Since 1T-$CrTe_2$ is ferromagnetic, the exchange coupling constants J_{xy} and J_z are positive. For perpendicular magnetic anisotropy in a monolayer, K_u is positive. The spin magnetic moment $M_j^z = -g\mu_B S_j^z$, so that the last term is $-\frac{1}{N}\sum_j \mathbf{M}_j\cdot\mathbf{B}$ with $\mathbf{B}$ directed along the $\pm z$ direction. Exchange coupling is included for nearest neighbor Cr ions.

The magnon dispersion is determined by first performing the Holstein-Primakoff transformation [53] defined by the operator substitution $S_j^z = S - \hat{n}_j$, where $\hat{n}_j = a_j^\dagger a_j$ is the magnon number operator. One can then show that the spin ladder operators, $S_j^+ = S_j^x + iS_j^y$ and $S_j^- = S_j^x - iS_j^y$, are given by $S_j^+ = \sqrt{2S}\sqrt{1-\frac{\hat{n}_j}{2S}}\ a_j$, and $S_j^- = \sqrt{2S}a_j^\dagger\sqrt{1-\frac{\hat{n}_j}{2S}}$. At low temperatures such that $\langle\hat{n}_j\rangle \ll S$, one expands out the square root terms to first order in $\hat{n}_j$ to obtain

$$\begin{aligned}\hat{S}_j^z &= S - \hat{n}_j \\ \hat{S}_j^+ &\approx \sqrt{2S}\left(1-\frac{\hat{n}_j}{4S}\right)a_j \\ \hat{S}_j^- &\approx \sqrt{2S}a_j^\dagger\left(1-\frac{\hat{n}_j}{4S}\right)\end{aligned} \quad (5)$$

These are the equations used to transform the Hamiltonian in Eq. (10). Keeping terms to first order in $\hat{n}_j$, and substituting the Fourier representation of the operators $a_j = \frac{1}{\sqrt{N}}\sum_{\mathbf{k}} e^{-i\mathbf{k}\cdot\mathbf{R}_j}a_{\mathbf{k}}$ (see SM for details), the Hamiltonian governing the magnon dynamics is

$$H_m = \tfrac{2S}{N}\sum_{\mathbf{k}}\left[J_z Z + K_u - \tfrac{g\mu_B B_z}{2S} - J_{xy}\mathrm{Re}\{f(\mathbf{k})\}\right]a_{\mathbf{k}}^\dagger a_{\mathbf{k}}, \quad (6)$$

where $Z = 6$ is the number of nearest neighbor Cr atoms, and $f(\mathbf{k}) \equiv \sum_{\boldsymbol{\delta}} e^{-i\mathbf{k}\cdot\boldsymbol{\delta}} \in \mathbb{R}$ is the form factor resulting from the sum over the 6 nearest Cr neighbors located at the vertices of the hexagon given explicitly by $f(\mathbf{k}) = 2\left[\cos(k_x a) + 2\cos\left(\frac{k_x a}{2}\right)\cos\left(\frac{\sqrt{3}}{2}k_y a\right)\right]$. In the limit of small ka, the magnon energy given by Eq. (6) reduces to

$$E_m(k) = 12S\,(J_z - J_{xy}) + 2SK_u - g\mu_B B_z + 3SJ_{xy}k^2a^2. \quad (7)$$

The parameters J_{xy}, J_z, and K_u are extracted from the DFT calculated total energies of structures with different spin configurations as shown in Fig. 7. From the Hamiltonian of Eq. (4), the total energies for each spin configuration for two unit cells (2 Cr atoms) are $E_{FM,z} = 24S^2J_z + 2S^2K_u + E_0$, $E_{AFM,z} = -4S^2J_z + 2S^2K_u + E_0$,

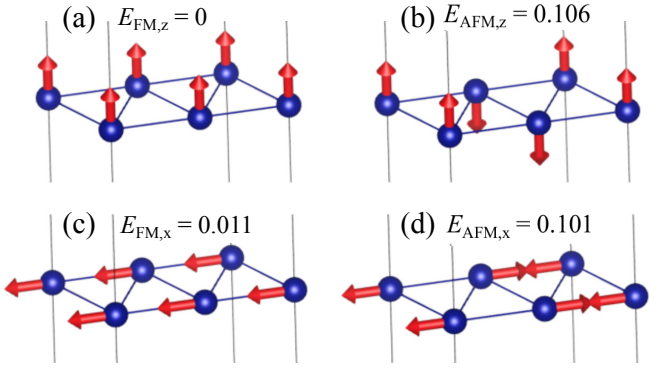

FIG. 7. Different spin configurations in a $2\times1\times1$ supercell, showing only the Cr atoms, used for determining the exchange and anisotropy parameters in Eq. (4). The 2×1 supercell is shown with the solid black line. Nearest neighbors for the 2 atoms in the supercell are shown with the thinner blue lines. The total energy (in eV) with respect to $E_{FM,z}$ is shown for each spin configuration.

$E_{FM,x} = 12S^2J_{xy} + E_0$, and $E_{AFM,x} = -4S^2J_{xy} + E_0$. The exchange and anisotropy constants are then

$$\begin{aligned}J_{xy} &= (E_{FM,x} - E_{AFM,x})/(16S^2) \\ J_z &= (E_{FM,z} - E_{AFM,z})/(16S^2) \\ K &= (E_{FM,z} - E_{FM,x} - 12J_zS^2 - 12J_{xy}S^2)/(2S^2).\end{aligned} \quad (8)$$

The values obtained with $U = 5.8$ eV are $J_z = 2.93$ meV, $J_{xy} = 2.50$ meV, and $K_u = -0.0959$ meV.

Eq. (7) shows that the effective anisotropy governing the spin gap in the magnon dispersion is

$$K_{\text{eff}} = (J_z - J_{xy})Z + K_u = 2.49\ (\text{meV}). \quad (9)$$

We can confirm the assumption that the dipolar energy can be neglected, since an estimate for the magnitude of the dipolar energy is $\frac{\mu_0}{2}M_s^2 = \frac{\mu_0}{2}(g\mu_B S)^2 V_{uc} = 41\ \mu$eV, where V_{uc} is the volume of one unit cell. This is one order of magnitude smaller than the effective anisotropy energy. With the definition of K_{eff}, the XXZ Hamiltonian of Eq. (4) maps onto a Heisenberg Hamiltonian with isotropic exchange and single-ion anisotropy as

$$H = \tfrac{-J}{N}\sum_{i\neq j}\mathbf{S}_i\cdot\mathbf{S}_j - \tfrac{K_{\text{eff}}}{N}\sum_j (S_j^z)^2 + g\mu_B B_z\tfrac{1}{N}\sum_j S_j^z, \quad (10)$$

where $J = J_{xy}$, and the low energy magnon dispersion becomes

$$E_m(k) = 2SK_{\text{eff}} - g\mu_B B_z + 3SJk^2a^2. \quad (11)$$

Since the effect of anisotropic exchange and single ion anisotropy enter the equations governing the observables of magnetic anisotropy and magnon dispersion in exactly the same way, experimental measurements of effective anisotropy energies, spin-wave gaps, and the resulting transition temperatures do not help to separate

these two effects. However, the experimental measurements of effective anisotropy and transition temperature can shed light on the relative magnitudes of J and $K_{\rm eff}$. Two seperate experimental investigations extracted effective anisotropy constants from magnetization versus field curves of $K_{\rm exp} = 5.6$ Merg/cm^3 $= 0.26$ meV/u.c., where, for the conversion, we use the volume of the bulk unit cell [17, 21]. The experimentally measured Curie temperatures of few layer 1T-$CrTe_2$ range from $T_c \sim 200 - 300$ K [16–19]. From the value of $K_{\rm exp}$ and the range of values for T_c, we can extract a range of values for J using renormalized spin wave theory (RSWT) [34, 38, 54].

Starting from the operator identity $S_j^z = S - \hat{n}_j$ and the saturation magnetization per unit cell $M_s = g\mu_B S$, the expected value of the magnetization as a function of temperature is

$$M(T) = M_s - g\mu_B \frac{1}{N} \sum_{\mathbf{k}} \langle \hat{n}_{\mathbf{k}} \rangle \tag{12}$$

where $\langle \hat{n}_{\mathbf{k}} \rangle = [e^{E_m(k)/k_BT} - 1]^{-1}$ is given by the Bose-Einstein factor. The renormalization is included by replacing S in the dispersion relation by $S - \frac{1}{N}\sum_{\mathbf{k}} \langle \hat{n}_{\mathbf{k}} \rangle = \frac{M(T)}{g\mu_B}$. With this substitution, and using the expression for the low-energy dispersion (Eq. (11)), the equation for $M \equiv M(T)$ in units of μ_B becomes

$$M = M_s - \frac{gA_{uc}}{2\pi} \int_0^{k_{max}} dk \, \frac{k}{e^{\frac{M}{g}(2K_{\rm eff} + 3Jk^2a^2)/k_BT} - 1}, \tag{13}$$

where the sum over the two dimensional wavevector is converted into an integral, $A_{uc} = a^2\sqrt{3}/2$ is the area of a unit cell, and k_{max} is chosen to match the area of the first Brillouin zone, i.e. $\pi k_{max}^2 = \left(\frac{4\pi}{3a}\right)^2 \sqrt{3}/2$. Performing the integral gives

$$\frac{M}{g} = \frac{M_s}{g} - \frac{\sqrt{3}k_BT}{24\pi \frac{M}{g} J} \ln\left[\frac{1 - e^{-E_{\rm max}/k_BT}}{1 - e^{-E_{\rm min}/k_BT}}\right] \tag{14}$$

where $E_{\rm min} = 2\frac{M}{g}K_{\rm eff}$ and $E_{\rm max} = E_{\rm min} + \frac{8\pi}{\sqrt{3}}\frac{M}{g}J$.

Eq. (14) is solved for M, and $M(T)$ is plotted versus T in Fig. 8 with $J = 2.5$ meV and four different values of $K_{\rm eff}$. The solid red curve with $T_c = 405$ K results from the DFT calculated parameters of $K_{\rm eff} = 2.49$ meV and $J = 2.50$ meV. The other curves show the effect of reducing $K_{\rm eff}$. As $K_{\rm eff}$ is reduced by factors or 2, 5, and 10, T_c decreases from 405 K to 311 K, 234 K, and 197 K, respectively. These curves illustrate the sensitivity of T_c to the parameters J and $K_{\rm eff}$.

The pairs of parameters J and $K_{\rm eff}$ that result in a given value for T_c form a curve in the two dimensional $J - K_{\rm eff}$ parameter space. We solve for that curve by setting $T = T_c$ and $M = 1.65\mu_B$ in Eq. (14). The value of $M = 1.65\mu_B$ is chosen, since we find it to be at the point, or extremely close to the point, where the maximum temperature occurs in all of the $M(T)$ versus T curves such as those shown in Fig. 8. The $J - K_{\rm eff}$

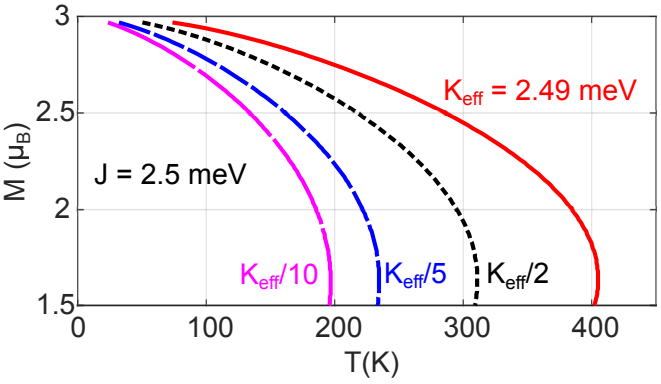

FIG. 8. Magnetization versus temperature with $J = 2.5$ meV and four different values of $K_{\rm eff}$ as shown on the plot.

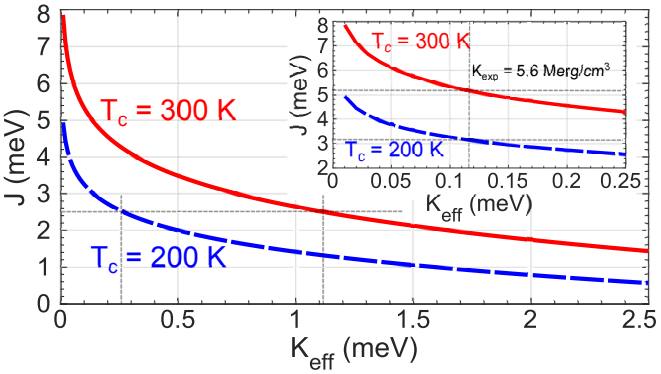

FIG. 9. Values of J and $K_{\rm eff}$ that result in $T_c = 300$ K and 200 K calculated from Eq. (14). Inset: Enlarged view for small $K_{\rm eff}$. To convert to values for experimentally determined anisotropy, $K_{\rm exp} = S^2 K_{\rm eff} = 2.25 K_{\rm eff}$ (see Supplemental Material (SM) [46] and references [17, 55] therein). The vertical dashed line in the inset designates the experimentally measured $K_{\rm exp} = 5.6$ Merg/cm^3.

curves showing all parameter pairs resulting in $T_c = 200$ K and $T_c = 300$ K calculated from Eq. (14) are shown in Fig. 9.

The one experimental value of $K_{\rm exp} = 5.6$ Merg/cm^3 is marked by the dashed vertical line on the inset. The experimentally measured range of T_c values between 200 K and 300 K then provides a range of J values between 3.1 meV and 5.2 meV. The dashed horizontal line on the main plot shows the DFT calculated value of $J = 2.5$ meV, which is slightly below the minimum extracted value from the experimental data. The calculated $K_{\rm eff} = (J_z - J_{xy})Z = 2.5$ meV is too large. It is a result of the large value of magnetic anisotropy energy, $\Delta_{\rm MA} = 5.56$ meV, and the large coordination number, $Z = 6$. We note that our values for $\Delta_{\rm MA}$ are similar to and somewhat less than those calculated in Ref. [18] with similar values of U.

Care is required when comparing to other values for $K_{\rm eff}$ and J in the literature. Some authors define their Heisenberg Hamiltonian as $\frac{J'}{2}\sum_{i \neq j} \mathbf{S}_i \cdot \mathbf{S}_j$ [34, 56], in

which case, their values for J must be scaled by a factor of 2 for comparison with our values. Many authors set $S = 1$ when extracting exchange constants from the DFT total energy calculations [27, 29] while other authors do not [34, 56]. Values for J' calculated with $S = 1$ must be scaled by S^2 to compare with our values for J, i.e. $J = J'/S^2$. The same also holds true for the anisotropy constant K. Below, we compare to other values in the literature appropriately scaled (i.e. by a factor of $\frac{1}{2}$ or by a factor of $S^2 = \frac{9}{4}$) to match the definition of our values, and we also convert to our sign convention in which positive J and K values correspond to FM coupling and PMA, respectively. Based on PBE+U = 2 eV total energy calculations of ML 1T-$CrTe_2$ and fitting to a symmetric second neighbor Heisenberg model with single-ion anisotropy, Ref. [27] found a nearest neighbor exchange interaction of J_1 = 5.9 meV, a second neighbor interaction of J_2 = 1.1 meV, and an anisotropy constant of $K = -0.46$ meV. We note the large value of J_1, however, since the magnetic anisotropy is in-plane, RSWT predicts $T_c = 0$ K. As noted above, ML CrI_3 has many similarities to ML $CrTe_2$ such as octahedral coordination, anions with large SOC, and PMA. PBE+U = 2.7 eV calculations of ML CrI_3 found J = 1.1 meV and K_{eff} = 0.045 meV [34]. The lower values are consistent with the lower value of T_c for CrI_3 with respect to that of $CrTe_2$. In general, the exchange constants straddle the ones predicted from experimental data analysed with RSWT. The predicted anisotropy constants tend to have a stronger dependence and even change sign depending on the value of U.

IV. CONCLUSIONS

In this study, we performed a systematic first principle DFT calculations of the structural, electronic, and magnetic properties of various phases of $CrTe_2$. A comparison of the formation energies of the different phases of $CrTe_2$ show that the 1T-$CrTe_2$ phase is the ground state. For the bulk and monolayer, the formation energy of the 1T phase lies 0.30 eV and 0.11 eV per formula unit below the next metastable phase, respectively. Furthermore, NEB calculations show that the energy barriers separating the phases are large, on the order of 0.5 eV for both the bulk and monolayer. Based on the linear response method, the calculated U value for the Cr atom in 1T-$CrTe_2$ is 5.8 eV. The magnetic anisotropy of 1T-$CrTe_2$ originates from the SOC of the Te atoms and the superexchange coupling between the Cr-3d and Te-5p orbitals. For any number of layers ($n \geq 2$) of 1T-$CrTe_2$, the magnetic moment lies in-plane, however for a monolayer, the magnetic moment is out-of-plane. Band filling with a sheet carrier concentration more than $n_s = 1.5 \times 10^{14}$ cm^{-2} or a tensile bi-axial strain of 3% can cause the magnetic easy axis of monolayer 1T-$CrTe_2$ switch from out-of-plane to in-plane. Compressive bi-axial strain of -3%, causes the magnetic easy axis of bilayer 1T-$CrTe_2$ to switch from in-plane to out-of-plane. PMA is favored in structures with smaller dihedral angles consistent with the trend identified previously for CrI_3. A RSWT analysis using experimental values for magnetic anisotropy and T_c, provides a range of expected values for the nearest neighbor exchange constant lying between 3.1 meV and 5.2 meV for values of T_c in the range of 200 K and 300 K, respectively.

ACKNOWLEDGMENTS

This work was supported in part by the U.S. Army Research Laboratory (ARL) Research Associateship Program (RAP) Cooperative Agreement(CA) W911NF-16-2-0008. This work used the Extreme Science and Engineering Discovery Environment (XSEDE) [57], which is supported by National Science Foundation Grant No. ACI-1548562 and allocation ID TG-DMR130081. YL acknowledges helpful discussions with Prof. Ran Cheng.

REFERENCES

[1] B. Huang, G. Clark, E. Navarro-Moratalla, D. R. Klein, R. Cheng, K. L. Seyler, D. Zhong, E. Schmidgall, M. A. McGuire, D. H. Cobden, W. Yao, D. Xiao, P. Jarillo-Herrero, and X. Xu, Layer-dependent ferromagnetism in a van der Waals crystal down to the monolayer limit, Nature **546**, 270 (2017).

[2] C. Gong, L. Li, Z. Li, H. Ji, A. Stern, Y. Xia, T. Cao, W. Bao, C. Wang, Y. Wang, Z. Q. Qiu, R. J. Cava, S. G. Louie, J. Xia, and X. Zhang, Discovery of intrinsic ferromagnetism in two-dimensional van der Waals crystals, Nature **546**, 265 (2017).

[3] I. J. Park, S. Kwon, and R. K. Lake, Effects of filling, strain, and electric field on the Néel vector in antiferromagnetic CrSb, Phys. Rev. B **102**, 224426 (2020).

[4] L. Websterand J.-A. Yan, Strain-tunable magnetic anisotropy in monolayer $CrCl_3$, $CrBr_3$, and CrI_3, Phys. Rev. B **98**, 144411 (2018).

[5] Y. Song, X. Wang, and W. Mi, Role of electron filling in the magnetic anisotropy of monolayer WSe_2 doped with 5*d* transition metals, Phys. Rev. Materials **1**, 074408 (2017).

[6] X. Kong, H. Yoon, M. J. Han, and L. Liang, Switching interlayer magnetic order in bilayer CrI_3 by stacking reversal, Nanoscale **13**, 16172 (2021).

[7] Y. Xie, Y. Yuan, M. Birowska, C. Zhang, L. Cao, M. Wang, J. Grenzer, D. Kriegner, P. Doležal, Y.-J. Zeng, X. Zhang, M. Helm, S. Zhou, and S. Prucnal, Strain-induced switching between noncollinear and collinear spin configuration in magnetic Mn_5Ge_3 films, Phys. Rev. B **104**, 064416 (2021).

[8] M. Xu, C. Huang, Y. Li, S. Liu, X. Zhong, P. Jena, E. Kan, and Y. Wang, Electrical control of magnetic phase transition in a Type-I multiferroic double-metal trihalide monolayer, Phys. Rev. Lett. **124**, 067602 (2020).

[9] H. Wang, J. Qi, and X. Qian, Electrically tunable high curie temperature two-dimensional ferromagnetism in

van der Waals layered crystals, Applied Physics Letters **117**, 083102 (2020).
[10] K. L. Seyler, D. Zhong, B. Huang, X. Linpeng, N. P. Wilson, T. Taniguchi, K. Watanabe, W. Yao, D. Xiao, M. A. McGuire, K.-M. C. Fu, and X. Xu, Valley manipulation by optically tuning the magnetic proximity effect in WSe_2/CrI_3 heterostructures, Nano Letters **18**, 3823 (2018).
[11] J. Liuand T. Hesjedal, Magnetic topological insulator heterostructures: A review, Advanced Materials , 2102427 (2021).
[12] M. Och, M.-B. Martin, B. Dlubak, P. Seneor, and C. Mattevi, Synthesis of emerging 2D layered magnetic materials, Nanoscale **13**, 2157 (2021).
[13] C. Ataca, H. Sahin, and S. Ciraci, Stable, single-layer MX_2 transition-metal oxides and dichalcogenides in a honeycomb-like structure, The Journal of Physical Chemistry C **116**, 8983 (2012).
[14] H. Guo, N. Lu, L. Wang, X. Wu, and X. C. Zeng, Tuning electronic and magnetic properties of early transition-metal dichalcogenides via tensile strain, The Journal of Physical Chemistry C **118**, 7242 (2014).
[15] D. C. Freitas, R. Weht, A. Sulpice, G. Remenyi, P. Strobel, F. Gay, J. Marcus, and M. Núñez-Regueiro, Ferromagnetism in layered metastable 1T-$CrTe_2$, Journal of Physics: Condensed Matter **27**, 176002 (2015).
[16] X. Sun, W. Li, X. Wang, Q. Sui, T. Zhang, Z. Wang, L. Liu, D. Li, S. Feng, S. Zhong, *et al.*, Room temperature ferromagnetism in ultra-thin van der waals crystals of 1T-$CrTe_2$, Nano Research **13**, 3358 (2020).
[17] X. Zhang, Q. Lu, W. Liu, W. Niu, J. Sun, J. Cook, M. Vaninger, P. F. Miceli, D. J. Singh, S.-W. Lian, *et al.*, Room-temperature intrinsic ferromagnetism in epitaxial $CrTe_2$ ultrathin films, Nature communications **12**, 2492 (2021).
[18] L. Meng, Z. Zhou, M. Xu, S. Yang, K. Si, L. Liu, X. Wang, H. Jiang, B. Li, P. Qin, *et al.*, Anomalous thickness dependence of curie temperature in air-stable two-dimensional ferromagnetic 1T-$CrTe_2$ grown by chemical vapor deposition, Nature communications **12**, 809 (2021).
[19] Y. Sun, P. Yan, J. Ning, X. Zhang, Y. Zhao, Q. Gao, M. Kanagaraj, K. Zhang, J. Li, X. Lu, Y. Yan, Y. Li, Y. Xu, and L. He, Ferromagnetism in two-dimensional crte2 epitaxial films down to a few atomic layers, AIP Advances **11**, 035138 (2021).
[20] C. M. O. Bastos, R. Besse, J. L. F. Da Silva, and G. M. Sipahi, Ab initio investigation of structural stability and exfoliation energies in transition metal dichalcogenides based on Ti-, V-, and Mo-group elements, Phys. Rev. Materials **3**, 044002 (2019).
[21] Y. Fujisawa, M. Pardo-Almanza, J. Garland, K. Yamagami, X. Zhu, X. Chen, K. Araki, T. Takeda, M. Kobayashi, Y. Takeda, C. H. Hsu, F. C. Chuang, R. Laskowski, K. H. Khoo, A. Soumyanarayanan, and Y. Okada, Tailoring magnetism in self-intercalated $Cr_{1+\delta}Te_2$ epitaxial films, Phys. Rev. Materials **4**, 114001 (2020).
[22] J.-J. Xian, C. Wang, J.-H. Nie, R. Li, M. Han, J. Lin, W.-H. Zhang, Z.-Y. Liu, Z.-M. Zhang, M.-P. Miao, Y. Yi, S. Wu, X. Chen, J. Han, Z. Xia, W. Ji, and Y.-S. Fu, Spin mapping of intralayer antiferromagnetism and field-induced spin reorientation in monolayer crte2, Nature Communications **13**, 257 (2022).
[23] J. P. Perdew, K. Burke, and M. Ernzerhof, Generalized gradient approximation made simple, Phys. Rev. Lett. **77**, 3865 (1996).
[24] H. Y. Lv, W. J. Lu, D. F. Shao, Y. Liu, and Y. P. Sun, Strain-controlled switch between ferromagnetism and antiferromagnetism in 1T-$CrTe_2$ (X=Se, Te) monolayers, Phys. Rev. B **92**, 214419 (2015).
[25] K. Schwarzand P. Blaha, Solid state calculations using WIEN2k, Computational Materials Science **28**, 259 (2003), proceedings of the Symposium on Software Development for Process and Materials Design.
[26] A. Otero Fumega, J. Phillips, and V. Pardo, Controlled two-dimensional ferromagnetism in 1T-$CrTe_2$: The role of charge density wave and strain, The Journal of Physical Chemistry C **124**, 21047 (2020).
[27] S. Li, S.-S. Wang, B. Tai, W. Wu, B. Xiang, X.-L. Sheng, and S. A. Yang, Tunable anomalous hall transport in bulk and two-dimensional 1T-$CrTe_2$: A first-principles study, Phys. Rev. B **103**, 045114 (2021).
[28] A. Li, W. Zhou, S. Peng, Y. Wang, M. Long, and F. Ouyang, Half-metallicity and enhanced magnetism in monolayer 1T-$CrTe_2$ by lithium adsorption, Physics Letters A **394**, 127195 (2021).
[29] P. Gao, X. Li, and J. Yang, Thickness dependent magnetic transition in few layer 1T phase $CrTe_2$, The Journal of Physical Chemistry Letters **12**, 6847 (2021).
[30] J. c. v. Klimeš, D. R. Bowler, and A. Michaelides, Van der waals density functionals applied to solids, Phys. Rev. B **83**, 195131 (2011).
[31] G. Kresseand J. Furthmüller, Efficient iterative schemes for ab initio total-energy calculations using a plane-wave basis set, Phys. Rev. B **54**, 11169 (1996).
[32] G. Kresseand J. Hafner, Ab initio molecular dynamics for liquid metals, Phys. Rev. B **47**, 558 (1993).
[33] Q.-Q. Li, S. Li, D. Wu, Z.-K. Ding, X.-H. Cao, L. Huang, H. Pan, B. Li, K.-Q. Chen, and X.-D. Duan, Magnetic properties manipulation of $CrTe_2$ bilayer through strain and self-intercalation, Applied Physics Letters **119**, 162402 (2021).
[34] J. L. Ladoand J. Fernández-Rossier, On the origin of magnetic anisotropy in two dimensional CrI_3, 2D Materials **4**, 035002 (2017).
[35] D.-H. Kim, K. Kim, K.-T. Ko, J. Seo, J. S. Kim, T.-H. Jang, Y. Kim, J.-Y. Kim, S.-W. Cheong, and J.-H. Park, Giant magnetic anisotropy induced by ligand *ls* coupling in layered Cr compounds, Phys. Rev. Lett. **122**, 207201 (2019).
[36] N. D. Merminand H. Wagner, Absence of ferromagnetism or antiferromagnetism in one- or two-dimensional isotropic Heisenberg models, Phys. Rev. Lett. **17**, 1133 (1966).
[37] M. Bloch, Magnon renormalization in ferromagnets near the Curie point, Phys. Rev. Lett. **9**, 286 (1962).
[38] H. Wang, J. Qi, and X. Qian, Electrically tunable high curie temperature two-dimensional ferromagnetism in van der waals layered crystals, Applied Physics Letters **117**, 083102 (2020).
[39] P. E. Blöchl, Projector augmented-wave method, Phys. Rev. B **50**, 17953 (1994).
[40] G. Kresseand D. Joubert, From ultrasoft pseudopotentials to the projector augmented-wave method, Phys. Rev. B **59**, 1758 (1999).
[41] S. Grimme, J. Antony, S. Ehrlich, and H. Krieg, A consistent and accurate ab initio parametrization of den-

sity functional dispersion correction (DFT-D) for the 94 elements H-Pu, The Journal of Chemical Physics **132**, 154104 (2010).

[42] G. Henkelman, B. P. Uberuaga, and H. Jonsson, A climbing image nudged elastic band method for finding saddle points and minimum energy paths, The Journal of Chemical Physics **113**, 9901 (2000).

[43] X. Chen, Y. Liu, and B. Sanyal, Manipulation of electronic and magnetic properties of 3d transition metal (Cr, Mn, Fe) hexamers on graphene with vacancy defects: Insights from first-principles theory, The Journal of Physical Chemistry C **124**, 4270 (2020).

[44] S. L. Dudarev, G. A. Botton, S. Y. Savrasov, C. J. Humphreys, and A. P. Sutton, Electron-energy-loss spectra and the structural stability of nickel oxide: An LSDA+U study, Phys. Rev. B **57**, 1505 (1998).

[45] M. Cococcioniand S. de Gironcoli, Linear response approach to the calculation of the effective interaction parameters in the LDA + U method, Phys. Rev. B **71**, 035105 (2005).

[46] See Supplemental Material at for the details about the Hubbard parameter calcualtion which includes, magnetic moment per Cr atom, K-point convergence test, phonon spectra, magnon dispersion derivation, and parameters used in the Heisenberg Hamiltonian.

[47] J. Liu, Q. Sun, Y. Kawazoe, and P. Jena, Exfoliating biocompatible ferromagnetic Cr-trihalide monolayers, Phys. Chem. Chem. Phys. **18**, 8777 (2016).

[48] H. J. Monkhorstand J. D. Pack, Special points for brillouin-zone integrations, Phys. Rev. B **13**, 5188 (1976).

[49] L. Lin, P. Sherrell, Y. Liu, W. Lei, S. Zhang, H. Zhang, G. G. Wallace, and J. Chen, Engineered 2D transition metal dichalcogenides-a vision of viable hydrogen evolution reaction catalysis, Advanced Energy Materials **10**, 1903870 (2020).

[50] M. S. Sokolikovaand C. Mattevi, Direct synthesis of metastable phases of 2D transition metal dichalcogenides, Chem. Soc. Rev. **49**, 3952 (2020).

[51] J. Chang, J. Zhao, and Y. Ding, Anisotropic superexchange through nonmagnetic anions with spin-orbit coupling, The European Physical Journal B **93**, 159 (2020).

[52] E. E. Reinehrand W. Figueiredo, Anisotropic heisenberg ferromagnetic model in two dimensions, Phys. Rev. B **52**, 310 (1995).

[53] T. Holsteinand H. Primakoff, Field dependence of the intrinsic domain magnetization of a ferromagnet, Phys. Rev. **58**, 1098 (1940).

[54] D. Stanek, O. P. Sushkov, and G. S. Uhrig, Self-consistent spin-wave theory for a frustrated Heisenberg model with biquadratic exchange in the columnar phase and its application to iron pnictides, Phys. Rev. B **84**, 064505 (2011).

[55] M. T. Johnson, P. J. H. Bloemen, F. J. A. den Broeder, and J. J. de Vries, Magnetic anisotropy in metallic multilayers, Reports on Progress in Physics **59**, 1409 (1996).

[56] X. Lu, R. Fei, and L. Yang, Curie temperature of emerging two-dimensional magnetic structures, Phys. Rev. B **100**, 205409 (2019).

[57] J. Towns, T. Cockerill, M. Dahan, I. Foster, K. Gaither, A. Grimshaw, V. Hazlewood, S. Lathrop, D. Lifka, G. D. Peterson, R. Roskies, J. R. Scott, and N. Wilkins-Diehr, XSEDE: Accelerating scientific discovery, Computing in Science Engineering **16**, 62 (2014).